Tropical Cyclones Downscaled from Simulations with Very High Carbon Dioxide Levels

ROBERT L. KORTY

Texas A&M University, College Station, Texas

KERRY A. EMANUEL

Massachusetts Institute of Technology, Cambridge, Massachusetts

MATTHEW HUBER

Purdue University, West Lafayette, Indiana, and University of New Hampshire, Durham, New Hampshire

RYAN A. ZAMORA[a]

Texas A&M University, College Station, Texas

(Manuscript received 28 March 2016, in final form 27 August 2016)

ABSTRACT

A method to simulate thousands of tropical cyclones using output from a global climate model is applied to simulations that span very high surface temperatures forced with high levels of carbon dioxide (CO_2). The climatology of the storms downscaled from a simulation with modern-day conditions is compared to that of events downscaled from two other simulations featuring 8 and 32 times preindustrial-era levels of CO_2. Storms shift poleward with warming: genesis locations and track densities increase in subtropical and higher latitudes, and power dissipation increases poleward of 20°S and 30°N. The average latitude at which storms reach their maximum intensity shifts poleward by more than 1.5° latitude in the $8 \times CO_2$ experiment and by more than 7° latitude in the $32 \times CO_2$ case. Storms live longer and are more numerous in both of the warmer climates. These increases come largely from an expansion of the area featuring favorable conditions into subtropics and midlatitudes, with some regions of the Arctic having the thermodynamic conditions necessary to sustain systems in the hottest case. Storms of category 5 intensity are 52% more frequent in the $8 \times CO_2$ experiment but 40% less so in the $32 \times CO_2$ case, largely owing to a substantial decline in low-latitude activity associated with increases in a normalized measure of wind shear called the ventilation index. Changes in genesis and track densities align well with differences in the ventilation index, and environmental conditions become substantially more favorable poleward of about 20° latitude in the warmer climates.

1. Introduction

Many important characteristics of the tropical atmosphere expand poleward in simulations of warmer climates, and there is observational evidence that several properties of the general circulation have shifted in response to the warming of the last several decades. Among them are a widening of the Hadley circulation (Hu and Fu 2007; Seidel and Randel 2007; Seidel et al. 2008; Adam et al. 2014), an increase in the lateral extent of the low tropical values of total column ozone (Hudson et al. 2006), and poleward shifts in dry zones and midlatitude storm tracks (Mbengue and Schneider 2013; Barnes and Polvani 2013; Lucas et al. 2014; Simpson et al. 2014). Kossin et al. (2014, 2016) reported that the latitudes at which tropical storms reach their peak intensity have increased in recent decades. In a paleoclimate context, simulations of the warm Eocene epoch show a poleward expansion of the area dominated by moist adiabatic lapse rates (Korty and Emanuel 2007; Zamora et al. 2016), which are common to regions where tropical cyclones (TCs) form and intensify.

One important potential consequence of these shifts in the general circulation is that systems such as TCs, which are restricted by environmental conditions to parts of the globe with thermodynamic characteristics

[a] Current affiliation: Johns Hopkins University, Baltimore, Maryland.

Corresponding author e-mail: Robert L. Korty, korty@tamu.edu

DOI: 10.1175/JCLI-D-16-0256.1

suitable for them, may become viable in other climates in regions presently inhospitable to them. The climatology of TCs can respond not only directly to changes in external forcing but also indirectly through resulting shifts in the general circulation. Understanding the response of TCs to warmer climates is of significant practical importance, but it is also of fundamental interest to understand how TCs behave across a wide range of climates. Efforts to understand how TCs may respond to projections of climate changes over the next century have focused largely on analysis of model projections. These include analyses of the large-scale environmental factors known to favor genesis and intensification (e.g., Camargo et al. 2007), storms simulated directly in global climate models (e.g., Camargo 2013; Camargo and Wing 2016), and various downscaling techniques that simulate TCs using high-resolution models better suited to resolve storm structure and intensity (e.g., Knutson et al. 2015; Emanuel 2013).

Over the past decade, research on the response of TCs to projections of future climate change has shown that the frequency of the highest-intensity events is likely to increase with warming [see recent reviews by Walsh et al. (2016), Sobel et al. (2016), and Camargo and Wing (2016)] and that the latitude at which storms reach their peak intensity is likely to move poleward (Kossin et al. 2016). There is less confidence in how the total number of TCs may change. The downscaling method we use here has produced more storms in warmer climates (Emanuel 2013; Federov et al. 2010), but many models that directly simulate systems yield fewer storms with warming, largely from a reduction in the number of weak systems. Our understanding of frequency changes is limited by the lack of any theory that can predict even the order of magnitude of tropical cyclones observed in the present climate (Sobel et al. 2016).

We feel that these sets of results could profit from applying similar methods to simulations with much larger changes in external forcing than in those examined to date. This is partly to learn more about the behavior of the techniques themselves, but also to understand interactions between TCs and climate at a more fundamental level. Recent efforts with paleoclimate simulations have begun to consider how the conditions favorable for TCs differed at the Last Glacial Maximum, the middle Holocene, the Last Millennium, and the Pliocene (Federov et al. 2010; Korty et al. 2012a,b; Yan et al. 2015; Koh and Brierley 2015). These studies have shown that thermodynamic environments evolve with climate in complex ways, and any changes in TCs during these periods could affect remote climate and ocean heat storage and mixing (e.g., Mei et al. 2013; Thomas et al. 2014; Korty et al. 2008; Sriver and Huber 2007).

This paper focuses on the response of one downscaling method in simulations with very high levels of carbon dioxide and extremely hot ocean surfaces last seen during the very warm Miocene and Eocene epochs. We apply the downscaling method developed by Emanuel (2006; Emanuel et al. 2008) to simulations with the Community Atmosphere Model, version 3.0 (CAM3.0) forced with 8 and 32 times preindustrial-era levels of carbon dioxide (CO_2). The method, reviewed further in section 2, runs the axisymmetric model of Emanuel (1995) along thousands of synthetically generated tracks to examine the response to environmental conditions encountered along the paths. This technique has two distinct advantages: it is computationally efficient given that the axisymmetric model is phrased in angular momentum coordinates, which gives high spatial resolution in the core of the system (where it is needed to resolve intense events), and it overcomes the difficulties inherent with the smaller sample sizes of explicitly resolved cases. Importantly, it resolves the full distribution of possible intensities, a feat presently not possible with most directly simulated techniques.[1] One potential drawback is that the method ignores possibly important changes in the climatology of initial disturbances; implicitly, it assumes these are not rate limiting. Another limitation is that because the features are run offline, they cannot feed back on the underlying model in ways that actual systems may do in nature. Cold wakes from mixing thermocline waters to the surface (Price 1981) can alter the environment for a system that follows several days behind, and the length scale for storm separation may itself change with climate (e.g., Khairoutdinov and Emanuel 2013). Also, there are no effects of a storm's intensity on its track or effects of its size on movement. Still, the method permits study of some questions presently impossible in coarser models; namely, how do intensity distributions and other properties of the climatology respond to the different environmental conditions in other climates?

We review the details of the downscaling technique in the next section and present the properties of the climatology of the downscaled TCs in section 3. We consider their relationship to changes in large-scale environmental conditions in section 4 and discuss some implications of the findings in section 5.

2. Data and methods

We employ the downscaling technique developed by Emanuel (2006) and Emanuel et al. (2008), in which a large number [$O(10^6)$ are used here] of weak initial disturbances

[1] Global models, even with 0.25° resolution, typically yield truncated intensity distributions, although Murakami et al. (2015) showed success simulating category 4 and 5 events with 25-km horizontal resolution.

are randomly distributed over all oceans up to 80°N within the large-scale flows of global climate model output. This set of seeds is then advected by the model's tropospheric flow, defined by 250- and 850-hPa-level winds, and corrected for "beta drift" to form a set of tracks. (Any tracks approaching the North Pole are terminated at 87°N.) The axisymmetric model described by Emanuel (1995) and refined in Emanuel et al. (2004) to incorporate the effects of environmental wind shear and ocean coupling is run using environmental conditions along each of the synthetic tracks. A great majority of seeds fail to develop and are discarded; those that survive and intensify are added to the database examined here. This process is continued until a predetermined, large number of successful storms for each climate is obtained (9500 cases each here). The total number of seed vortices (both successful and failed) needed to reach this total is used to define the frequency for each climate (a larger number of failed cases prior to reaching the 9500th successful one translates to a lower annual frequency of events).

The global model simulations downscaled here were produced with CAM3.0 coupled to a slab ocean model with very high levels of carbon dioxide and were described earlier by Williams et al. (2009), Sherwood and Huber (2010), Caballero and Huber (2010, 2013), and Zamora et al. (2016). These are part of a set of simulations developed initially to study properties of past very warm geologic periods such as the Eocene epoch, but the specific set of experiments examined here retain modern-day continental configurations, including modern-day land surface–boundary conditions and aerosol levels. The only difference among them is the level of carbon dioxide, which ranges from 355 ppm (i.e., late-twentieth-century levels) in a control experiment (M-Ctrl) to several doublings of preindustrial-era levels: 2^3 times the preindustrial-era level of 280 ppm (i.e., 2240 ppm; M-3 experiment) and 2^5 times more (8960 ppm; M-5 experiment). We note that CAM3.0 exhibited lower climate sensitivity to doubling carbon dioxide than many other global models; the surface temperatures achieved in these simulations might be reached in a different model with higher climate sensitivity using lower levels of carbon dioxide than required here.

These simulations were computed at T42 spectral resolution (~2.5° latitude by 2.5° longitude) and were developed from previously equilibrated lower-resolution simulations that were extended forward at higher spatial resolution using a slab ocean with lateral heat fluxes derived from their earlier coupled runs (e.g., see Williams et al. 2009; Sherwood and Huber 2010; Caballero and Huber 2010, 2013). We downscale 19 years of 6 hourly data for each of the three climates. (Note that because the storms are simulated offline, this technique is not sensitive to the spatial resolution of the parent GCM unless its resolution affects the large-scale environmental factors that systems encounter.) The increasingly high levels of carbon dioxide lead to very warm surface temperatures, as displayed in Figs. 1a,c,e, which show the annual peak surface temperatures in each climate. Peak tropical sea surface temperatures (SSTs) rise from approximately 28°C in M-Ctrl to approximately 33°C in M-3 and to approximately 42°C in M-5. Some Arctic SSTs in M-5 reach 35°C (although the annual mean is substantially lower than these peak values here).

Emanuel (1986) showed that TCs are driven by an enthalpy flux from the ocean to the atmosphere, which is principally achieved in the form of evaporation; boundary layer parcels heated by this flux then redistribute the heat vertically through moist convection if the thermodynamic profile above permits. While thermodynamically favorable regions today are generally collocated with regions whose SST exceeds 26°C (Gray 1968), it has been known since at least the work of Emanuel (1987) that any correlation between SST and such conditions are climate specific. Korty et al. (2012a) showed that tropical cyclones were likely possible over waters with SST of 24°C at the Last Glacial Maximum, and Johnson and Xie (2010) and Hoyos and Webster (2012) also showed that the threshold for deep convection rises with warming.

The important consequence of this is that although temperatures found in regions that spawn TCs today expand poleward to much higher latitudes in these simulations, the regions that permit TCs move independently of any particular isotherm. Of potentially greater importance is the territorial expansion of air masses with moist neutral lapse rates over the extratropical oceans in warmer climates (Korty and Emanuel 2007; Zamora et al. 2016). The thermodynamic quantity potential intensity (PI) (Emanuel 1986; Bister and Emanuel 1998, 2002) provides an upper bound to the intensity a TC can achieve given the relationship between the surface temperature and environmental sounding above it; TCs cannot form or survive over regions of low PI, and these regions are usually coincident with stable air masses (e.g., see Korty et al. 2012b).

Figures 1b,d,f show the annual peak PI for each climate.[2] The area of high PI expands poleward in the

[2] We calculate PI using an algorithm based on the formulation of Bister and Emanuel (2002) but with a modification important for climates as far removed from modern conditions as those here: the pressure below which soundings are ignored during the iterative process of calculating convective available potential energy (CAPE) is lowered from 70 to 10 hPa as the height of the tropical tropopause in M-5 lifts to about 50 hPa (Zamora et al. 2016). Without this change, the level of neutral buoyancy that a parcel lifted from the surface could achieve would be capped arbitrarily, leading to spurious potential intensity values.

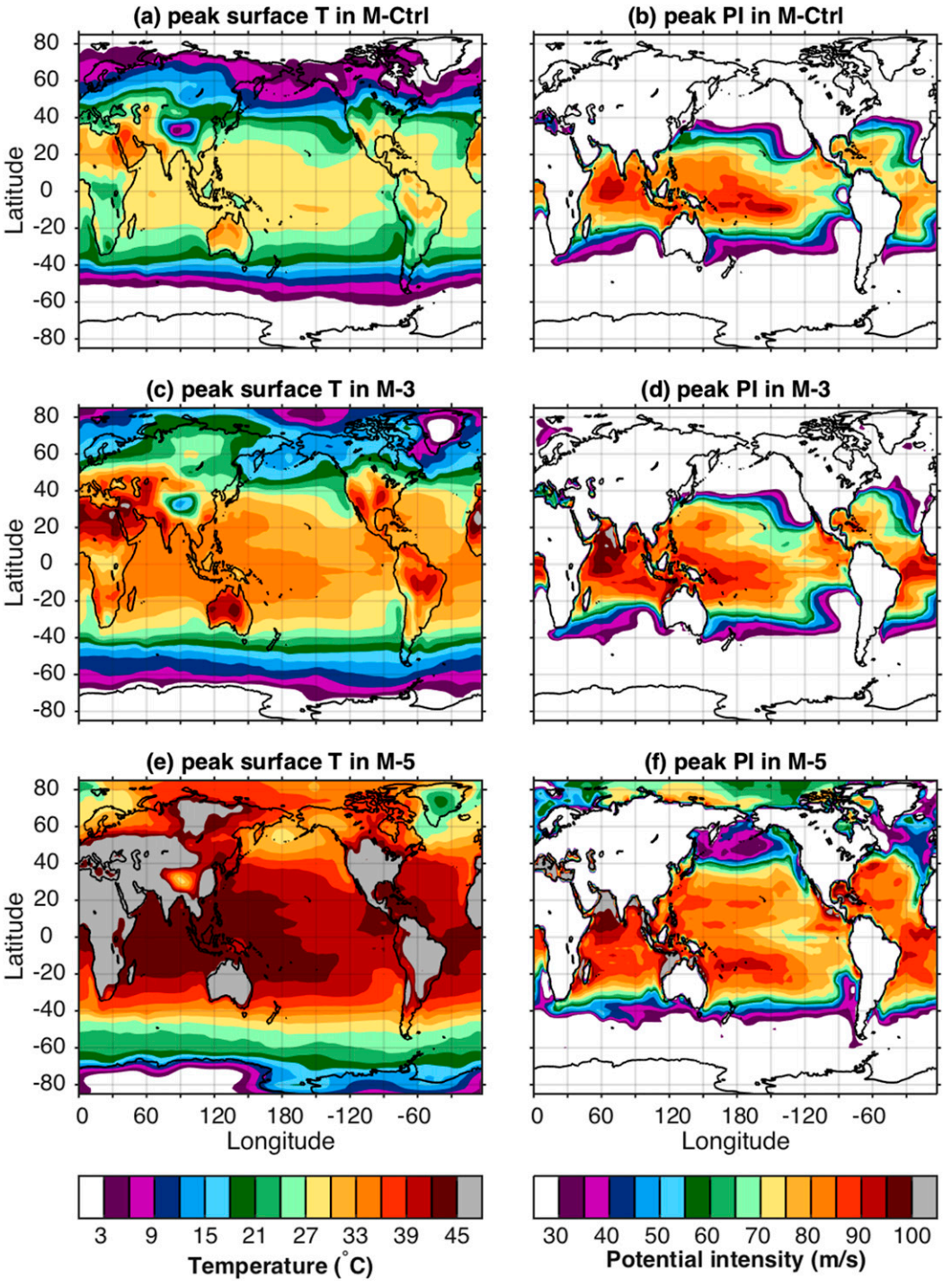

FIG. 1. (left) Annual peak surface temperature and (right) PI in (a),(b) M-Ctrl, (c),(d) M-3, and (e),(f) M-5.

warmer climates, reaching all the way into the Arctic in M-5. This expansion occurs concurrently with an increase in the frequency of air masses with moist adiabatic lapse rates reported by Zamora et al. (2016). Although surface temperatures rise to more than 42°C in the tropical Indian and western Pacific Oceans, typical PI values in the tropics are only slightly higher than in M-Ctrl. This is consistent with the analysis of Emanuel and Sobel (2013), who showed that PI approaches an upper limit in response to rising CO_2; they attributed

TABLE 1. Properties of the three climate experiments and of the global climatology of storms downscaled from them.

	M-Ctrl	M-3	M-5
CO_2 (ppmv)	355	2240	8960
Tropical mean SST (°C)	25.7	30.1	40.1
Global mean SST (°C)	17.1	22.9	29.3
No. of seeds used to yield 9500 storms	1 651 892	1 421 294	1 387 658
Annual frequency	90	105 (+16%)	108 (+20%)
Mean storm lifetime (days)	8.39	8.68 (+3%)	9.84 (+17%)
Mean $\lvert\phi_{\rm LMI}\rvert$	17.88°	19.46°	25.28°

this behavior to two causes. First, the temperature at the level of convective outflow also rises with CO_2 as the altitude at which convection terminates rises to significantly lower pressures. Second, and more importantly, the surface enthalpy flux increases slowly with rising CO_2 because the net upward longwave flux at the surface is already small at tropical SSTs, and the net surface longwave flux approaches zero at sufficiently high temperature (O'Gorman and Schneider 2008). The net effect is that PI rises modestly with warming from CO_2 beyond present-day values, and asymptotically approaches an upper limit as further increases in CO_2 pushed surface temperatures past about 32°C (Emanuel and Sobel 2013). We review this point further in section 4a.

Note that while peak SSTs in the northern Pacific and northern Atlantic in M-5 exceed 26°C and are warmer than in the tropics of the control run, PI here remains low owing to stable lapse rates aloft. This underscores the point above (and made first by Emanuel 1987) that PI is not a simple function of SST, and any correlation between a specific SST and high PI is likely climate specific. The area of high PI expands into the subtropics and some midlatitudes in the warmer climates, with values in the Arctic supporting TCs during July of M-5, as the thermodynamic soundings at these latitudes become more commonly moist adiabatic (as is the case throughout the tropics today). Values that exceed $100\,{\rm m\,s^{-1}}$ are rare in all climates, but areas adjacent to low-latitude land in M-3 and M-5 support them where desert air masses featuring superadiabatic lapse rates move over very hot ocean surfaces.

3. Results

These simulations offer an opportunity to examine the behavior of this downscaling technique over a much larger range of conditions than examined previously, and we now present how the climatology of TCs responds to these extreme conditions. The surface conditions seen in Fig. 1e are warmer than at any time since the early Eocene epoch (Caballero and Huber 2013), and Table 1 gives some properties of the simulations and global metrics of the TC climatology in each simulation. The annual frequency of events increases from M-Ctrl to M-3 but then shows little further increase in M-5. (These numbers are calibrated to have 90 total events in M-Ctrl and are calculated based on the number of seeds required to generate 9500 storms for each climate; using a larger numbers of seeds to generate a fixed number of events implies a lower frequency of genesis.) The mean storm lifetime rises modestly from M-Ctrl to M-3 but increases by about a day and a half in M-5. The latitude ϕ at which storms reach their lifetime maximum intensity (LMI) moves poleward by 1.58° latitude in M-3 and by 7.40° latitude in M-5. (We take the absolute value of all latitudes to include both the Northern and Southern Hemisphere.) A qualitatively similar poleward shift in $\lvert\phi_{\rm LMI}\rvert$ has been reported in the historical record and observed in simulations of anthropogenic climate changes (Kossin et al. 2014, 2016).

Figure 2 shows the genesis and track densities in the three climates. One of the most prominent changes is that the area in which TCs form expands to higher latitudes in M-3 and M-5, with a pronounced increase in genesis between 20° and 40°N in the hottest climate. A few events in M-5 form even in parts of the Arctic, an area inhospitable year-round in the control climate. The poleward shift in genesis in the Southern Hemisphere is less expansive, but a pronounced southward expansion occurs toward 20°S in the Indian Ocean, and some events between 20° and 30°S begin to appear in the southwestern Pacific, south-central Pacific, and South Atlantic. The track densities that follow from these points of genesis reach to increasingly high latitudes as the points of origin move poleward and the ability of systems to persist into higher latitudes increases in the warmer climates. Differences in both genesis and track densities between the two warmer climates and M-Ctrl are shown in Fig. 3. Although storms still form in the deep tropics in the two warmer climates (Figs. 2c,e), they do so less frequently than in M-Ctrl, with declines in some regions equatorward of 20°N and about 15°S in both experiments. Storm genesis expands poleward with warming, and tracks from these systems spread to even

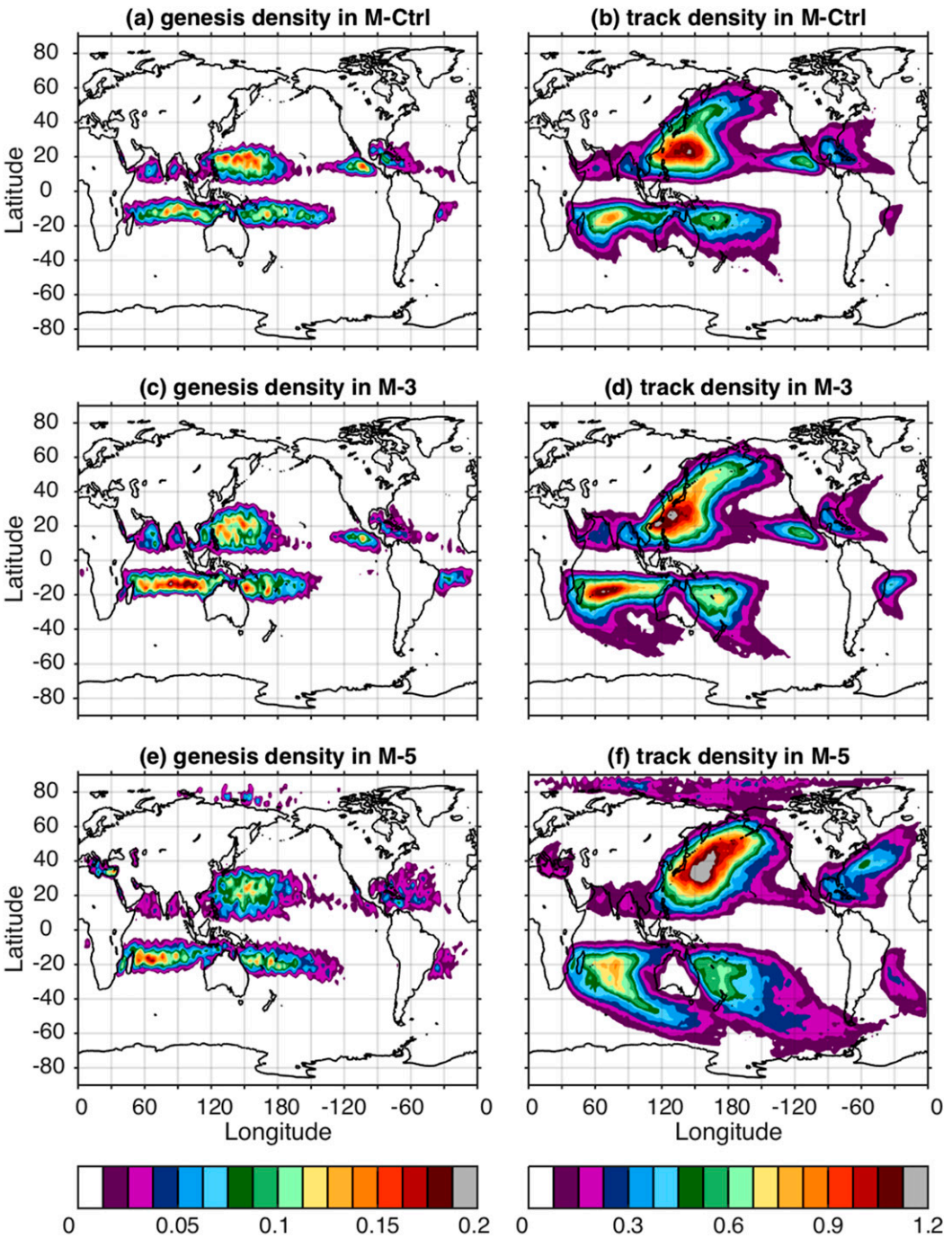

FIG. 2. (left) Genesis density and (right) track density in (a),(b) M-Ctrl, (c),(d) M-3, and (e),(f) M-5; units are number of events per year per 1° lat squared.

higher latitudes, consistent with the poleward shift in mean $|\phi_{\mathrm{LMI}}|$ reported in Table 1. There is a significant rise in track density throughout the midlatitudes of the North Pacific, North Atlantic (in M-5), and Southern Hemisphere oceans even though genesis remains largely confined to lower latitudes. (One exception to this is the development of some events in the Arctic during the summer months of M-5.)

The poleward shift in genesis is also evident in Fig. 4a, which plots the times and latitudes at which the zonally integrated genesis density exceeds 0.6 events per 1° latitude squared per year. There is a poleward expansion

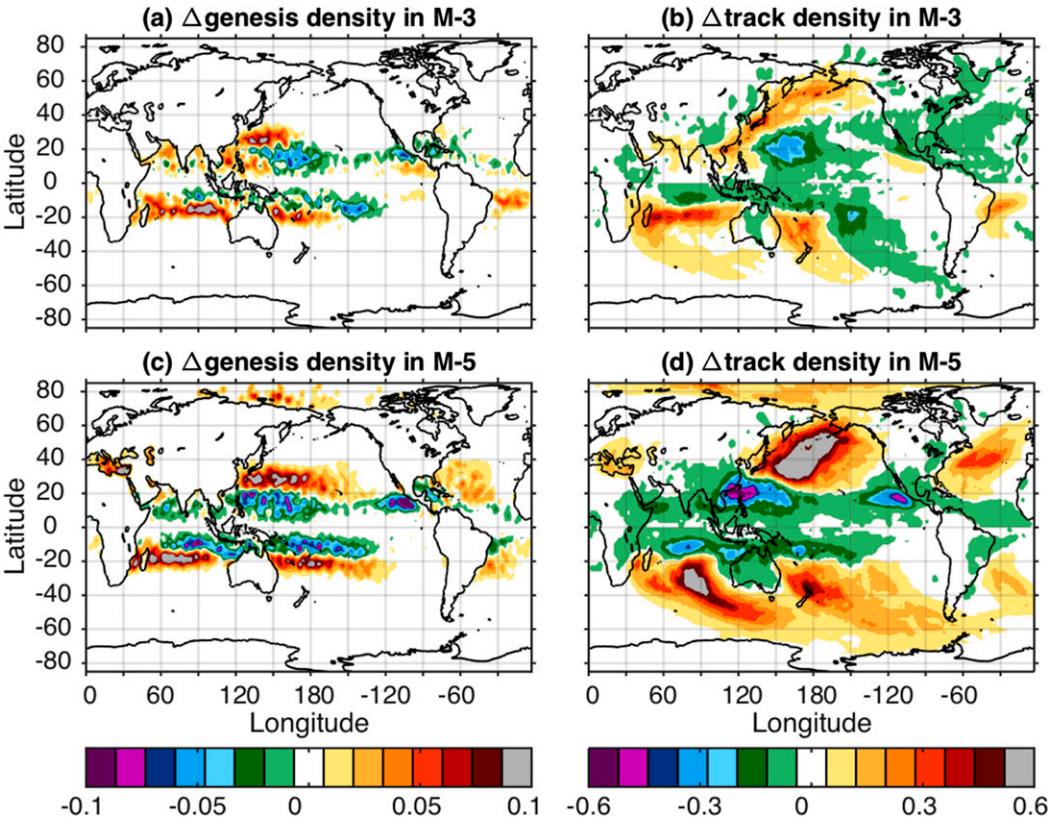

FIG. 3. (a) Difference in genesis density between M-3 and M-Ctrl. (b) Difference in track density between M-3 and M-Ctrl. (c),(d) As in (a),(b), but for differences between M-5 and M-Ctrl.

and migration of genesis regions, while lower latitudes in M-5 experience a decline in genesis. The range of months during which this level of genesis density occurs is similar in all three climates but contracts slightly in the hottest climate. In the Northern Hemisphere, significant genesis density begins about a month earlier in M-Ctrl than in the two warmer ones; the season ends in mid-November in all three. There is only a small difference in the Southern Hemisphere season between M-3 and M-Ctrl, but significant activity in M-5 ends in April, while modest amounts of activity in May continue in the other two. Figures 4b and 4c show the annual cycle in both hemispheres. The count is generally larger during the middle of each hemisphere's season in the two warmer climates but displays no consistent changes during the off-season months.

Regional changes in activity are given in Table 2, which shows the annual counts by basin. (Note that the numbers shown here include all storms that pass through each basin rather than only those that originate in it, so hemispheric and global totals differ from the sum of individual basins. Also, any increases in storm lifetimes can increase counts in multiple basins if a single storm traverses longer paths across boundaries.) Both hemispheres show an increase in activity with warming although the change in Southern Hemisphere activity is substantially larger in M-3 than is the more modest growth in Northern Hemisphere activity. There is variability in counts in the basins with smaller levels of activity (e.g., North Atlantic, eastern and central North Pacific, north Indian Ocean), but there is an increase in western North Pacific activity with warming while the eastern North Pacific frequency declines. In general, there is an increase in activity in nearly all basins from M-Ctrl to M-3, but the changes from M-3 to M-5 are more varied. Hemispheric and global counts also rise from M-Ctrl to M-3 with varied responses going from M-3 to M-5.

Figure 5a shows the distribution of maximum intensity in each climate binned by Saffir–Simpson wind-scale categories[3] and one additional column showing the more limited number of events that exceed 190 kt (1 kt $\approx$ 0.51 m s^{-1}). (Note that to show better the smaller numbers

[3] In operational practice, this categorization system is limited to the Western Hemisphere, but we apply these definitions globally here.

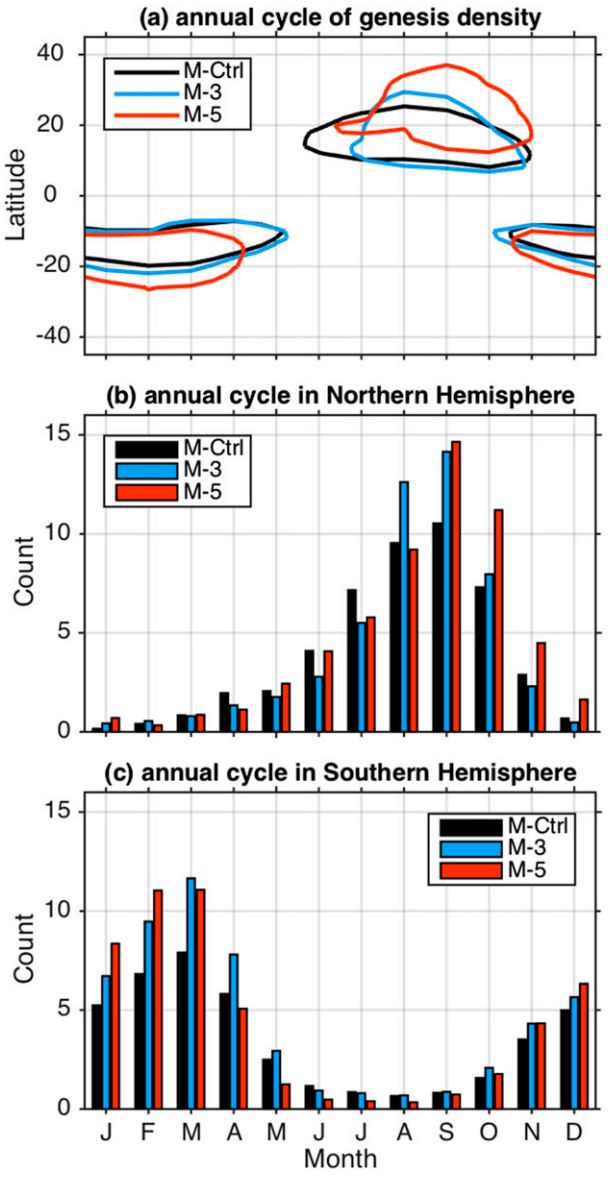

FIG. 4. (a) Annual and latitudinal distribution of genesis density exceeding 0.6 storms per year per 1° lat squared. (b) Annual cycle in the Northern Hemisphere in three climates. (c) As in (b), but for the Southern Hemisphere.

for higher-intensity categories, the axis showing annual frequencies is on a logarithmic scale.) The number of events in each storm category tapers with increasing intensity in M-Ctrl, with about a two-thirds of all events reaching hurricane intensity and about half of these reaching major hurricane intensities (defined as category 3 and stronger). The increase in frequency reported in Table 1 for M-3 comes from two ends of the intensity spectrum: a very large increase in the number of tropical storms that arise partly from an expansion of activity to higher latitudes and a 52% increase in the number of category 5 storms. There is a decline in the number of storms that reach peak intensity at categories 2 and 3 in M-3, which is similar to the behavior seen in recent historical trends analyzed by Holland and Bruyère (2014).

The number of tropical storms in M-5 is 121% larger than in M-Ctrl, primarily owing to a significant expansion of activity in subtropic latitudes, midlatitudes, and even some Arctic latitudes. Yet hurricanes of all intensities decline in frequency in M-5, with a 64% drop in the number of category 2–4 storms. The decline in the number of category 5 storms is smaller though still large (40%), while the most severe storms (those exceeding 190 kt) become 2.4 times more frequent than in the control case. The isolated number of events whose peak intensity exceeds 210 kt increases from about one storm every five years in M-Ctrl and M-3 to approximately one per year in M-5 (not shown). In fact, M-5 produced one hypercane (Emanuel 1987) that formed over the Caspian Sea and reached a peak velocity of 510 kt.

Figure 5b shows the area of significant track density for the subset of the event set with wind speed exceeding 137 kt, the threshold for category 5. In M-Ctrl, these areas are largely confined to the western North Pacific and to a band equatorward of 20°S in the Southern Hemisphere. In M-3, these expand northwest toward the coast of Asia, increase substantially in the southern Indian Ocean, expand poleward in both hemispheres, and appear in isolated pockets of the north Indian and Atlantic basins. In the hottest M-5 case, the area over which such winds can be found shifts poleward in both hemispheres while declining at lower latitudes. The area of category 5 winds reaches to 40°N in the western North Pacific and expands into subtropical latitudes in the southern Indian Ocean. These changes come from both a poleward expansion of the regions where storms begin and an increase in the number of tracks out of the expanded genesis regions to even higher latitudes (Fig. 2). Also, as we examine in the next section, the decrease in hurricane activity in tropical latitudes of M-5 occurs concurrently with environmental conditions becoming harsher for TC activity at low latitudes.

Power dissipation is an important cumulative metric of TC activity that depends on the integrated intensity, duration, and frequency of storm winds. An index of power dissipation, defined here as the integral over the lifetime τ of all storms of the maximum surface wind speed V cubed,

$$\mathrm{PDI} = \int_0^\tau V^3 \, dt, \tag{1}$$

is relevant to the aggregate effect tropical cyclones have on the ocean. (It is related to the work done by the wind

TABLE 2. Annual number of storms by region, hemisphere, and global total. The central North Pacific includes the area north of the equator between 180° and 140°W; the western North Pacific lies to its west and the eastern North Pacific to its east. The Australia region is defined as south of the equator between 90° and 160°E longitude; the southwest Indian Ocean is to its west and the South Pacific to its east. Note that data reported here include all storms that pass through a basin (including those that move into it rather than only those events that originate in it), so hemispheric and global totals differ from sum of data reported in individual basins.

	M-Ctrl	M-3	M-5
Global total	90	105 (+16%)	108 (+20%)
Northern Hemisphere	47.6	50.7 (+6%)	56.5 (+19%)
Southern Hemisphere	41.9	53.9 (+29%)	51.2 (+22%)
North Atlantic	6.51	5.68 (−13%)	9.79 (+50%)
Eastern North Pacific	8.46	8.17 (−3%)	6.47 (−24%)
Central North Pacific	7.90	8.70 (+10%)	16.7 (+111%)
Western North Pacific	30.0	32.4 (+8%)	33.9 (+13%)
Northern Indian Ocean	7.55	10.5 (+39%)	5.48 (−27%)
Southwest Indian Ocean	14.8	21.7 (+46%)	20.9 (+41%)
Australia region	18.5	23.7 (+28%)	20.5 (+11%)
South Pacific	16.1	16.0 (−0.4%)	21.1 (+31%)

on the ocean, which in turn supplies part of the energy available to mixing thermocline waters to the surface layer.) Increases in the number or duration of events tend to increase the metric, as they do with track density, but the cubic dependence on the surface wind speed makes it a strong function of changes in the frequency of the highest-intensity events. (An increase in the number of weak systems could have a strong influence on track density with only a minimal change in the cumulative power dissipated, for example.)

The power dissipation index (PDI) computed using (1) is $2.86 \times 10^{12}\,\mathrm{m^3\,s^{-2}}$ in M-Ctrl and increases 14% to $3.28 \times 10^{12}\,\mathrm{m^3\,s^{-2}}$ in M-3. The global integral declines 25% to $2.14 \times 10^{12}\,\mathrm{m^3\,s^{-2}}$ in M-5, but the locations where the power dissipation is largest shifts to higher latitudes in the hotter climates. Figure 6 presents the differences in PDI given by (1). In M-3, there is a northwestward shift toward the Asian coast in the western North Pacific and a poleward shift in the maxima in the Southern Hemisphere. In M-5, all tropical latitudes from about 20°S to about 25°N show less PDI than in M-Ctrl, but PDI increases substantially in the subtropics and midlatitudes. The shift in zonally integrated PDI is shown in Fig. 6c. (Note that its abscissa is linear in the sine of latitude.) This has important potential consequences as the amount of upper-ocean mixing that is induced by tropical cyclones rises with PDI (e.g., Sriver and Huber 2007; Korty et al. 2008), leading to possible feedbacks between TCs and climate (e.g., Federov et al. 2010) and ocean thermal structures (Sriver et al. 2008; Cheng et al. 2015). In the context of the early Cenozoic oceans, Thomas et al. (2014) showed that the best match between proxies of water mass distributions and numerical simulations occurred when substantially stronger ocean mixing was applied. These data suggest that TCs could provide an additional energy source during such periods.

To summarize our main results:

- TC activity moves poleward, with the mean latitude of lifetime maximum intensity shifting 1.58° poleward in M-3 and 7.40° poleward in M-5. Zonally integrated PDI shifts poleward with warming, with substantial increases in power dissipation in M-5 over the subtropics and midlatitudes poleward of 20°S and 25°N.
- Annual frequency is higher in both of the warmer climates. In M-3, both the number of tropical storms and the number of category 5 storms grow substantially, while the increase in M-5 comes entirely from tropical storms.
- The increase in the number of category 5 storms in M-3 is consistent with increases in intensity reported in anthropogenic warming (e.g., Sobel et al. 2016), but the decline in the hottest case examined (M-5) shows that this behavior may not continue indefinitely. The small upper end of the intensity distribution shows monotonic increases with warming: storms exceeding 190 kt become 66% more common in M-3 and 136% more common in M-5 than in the control case.

We examine the relationship between these differences in TC climatology and the underlying changes in large-scale environmental conditions in the next section.

4. Environmental conditions

Early work on tropical cyclones identified a set of environmental properties common to the regions that spawn and sustain the storms (Gray 1968, 1979), and we now consider how the results presented in the last

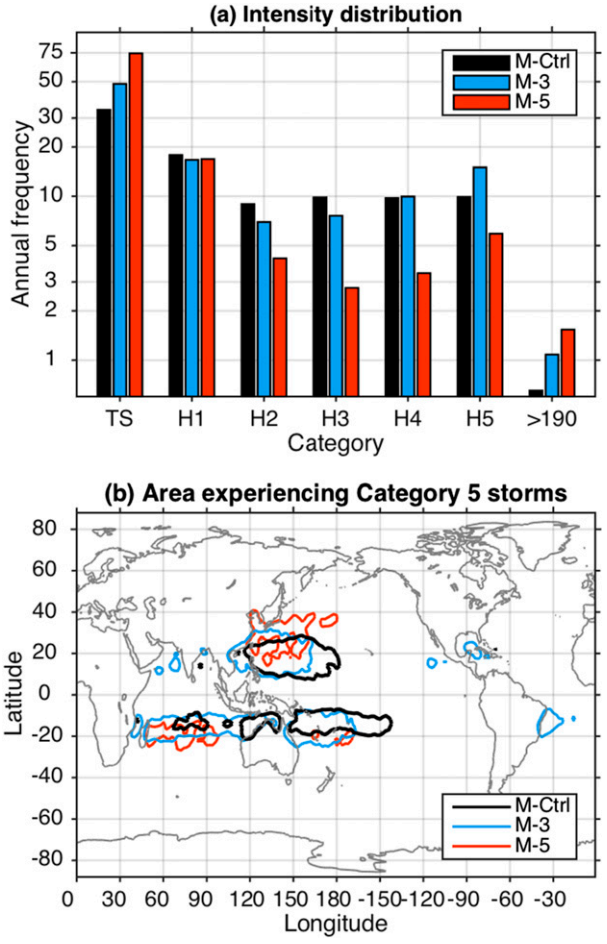

FIG. 5. (a) Annual frequency by Saffir–Simpson wind-scale categories [tropical storm (TS) through category 5 (H5)] with an additional column for events with peak intensities higher than 190 kt. Note logarithmic scale for plot. (b) Area that track density of category 5 winds (137 kt and higher) exceeds 0.02 storms per 1° lat squared.

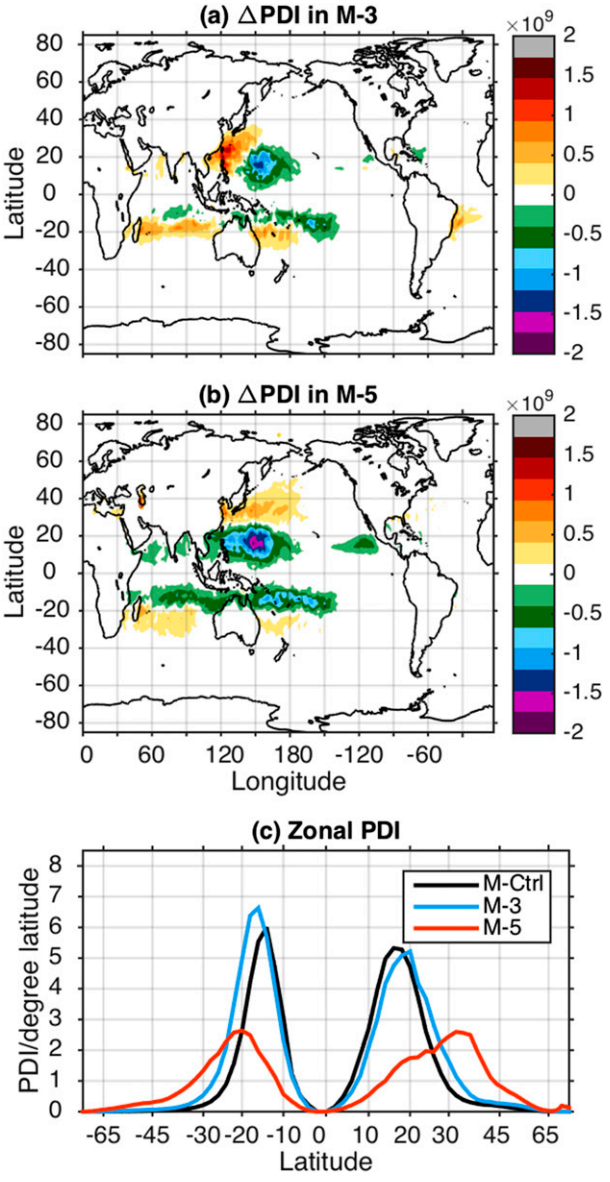

FIG. 6. (a) Difference in PDI between M-3 and M-Ctrl. (b) As in (a), but for difference between M-5 and M-Ctrl. (c) Zonal integral of PDI per 1° lat for M-Ctrl (black), M-3 (blue), and M-5 (red); note abscissa is linear in the sine of latitude.

section relate to them. While a large family of variables may accurately describe the conditions present in regions that support genesis in the modern climate, some specific formulations have proven most useful to predict correctly the response to altered conditions in different ones. These include potential intensity [in lieu of a threshold value of sea surface temperature, which is itself a function of climate (Emanuel 1987)], the ratio of tropospheric saturation deficits to surface thermodynamic equilibrium, and the strength of the vertical wind shear [see Emanuel et al. (2008) or Korty et al. (2012a) for further discussion]. Tang and Emanuel (2010, 2012) showed that these three parameters can be combined into a ventilation index, a normalized measure of wind shear that accounts for the humidity and thermodynamic properties of the environment. These parameters and their relationship to the changes in TC climatology are examined below.

a. *Potential intensity*

PI predicts an upper bound for intensity based on the thermodynamic environment at the sea surface and in the column of atmosphere above it (Emanuel 1986; Bister and Emanuel 2002). Yet it has also proven useful in another context: because its value is large only in regions where deep convection is possible (e.g., Korty et al. 2012a), it also serves to identify those regions

where environmental soundings can support the deep convection necessary to the existence of TCs at all.[4] Therefore, changes to this quantity are useful to address two important questions: 1) Does the upper bound on intensity change appreciably, and 2) does the areal coverage of high values change with climate?

The data presented in Fig. 1 show that while the areal coverage of the highest values of PI increases with warming, the largest value of PI in each climate is similar. Figure 7 shows the difference in storm-season mean PI between the two warmer climates and M-Ctrl. (In this and all subsequent plots, we define the storm season as July–October in the Northern Hemisphere and January–April in the Southern Hemisphere.[5] We base this on the consistency of the annual cycles across climates shown in Fig. 4.) The most substantial difference between the warmer climates and the control case is outside of the tropics, as the territory covered by high values of PI expands to the subtropics in M-3 and even to some midlatitudes and polar latitudes in M-5. There are also some important changes at low latitudes: the Atlantic, for example, features lower values in M-Ctrl, but they become as high as much of the western tropical Pacific in M-5. (Recall that TC activity also increases by 50% in the Atlantic in M-5; see Table 2.) Values of PI across the Pacific near the equator are no larger in M-3 or M-5 than they were in M-Ctrl and are in fact lower in the central equatorial Pacific where SSTs rise less than average for the tropics (Vecchi and Soden 2007). The poleward expansion of high PI values is qualitatively consistent with the poleward migration of genesis points reported in the last section, and the decrease in genesis density at the lowest latitudes in the central Pacific is consistent with the decrease in PI here. As noted earlier, Emanuel and Sobel (2013) found that PI saturates when surface warming results from increasing CO_2, a result that arises principally because the surface enthalpy flux increases slowly with rising CO_2 as the net upward longwave flux at the surface is already small at tropical SSTs, and the net surface longwave flux approaches zero at sufficiently high temperature (O'Gorman and Schneider 2008). We observe similar behavior in this general circulation model.

An upper bound on PI in a radiative–convective equilibrium state can be found by starting with the conventional expression for potential intensity V_{PI}:

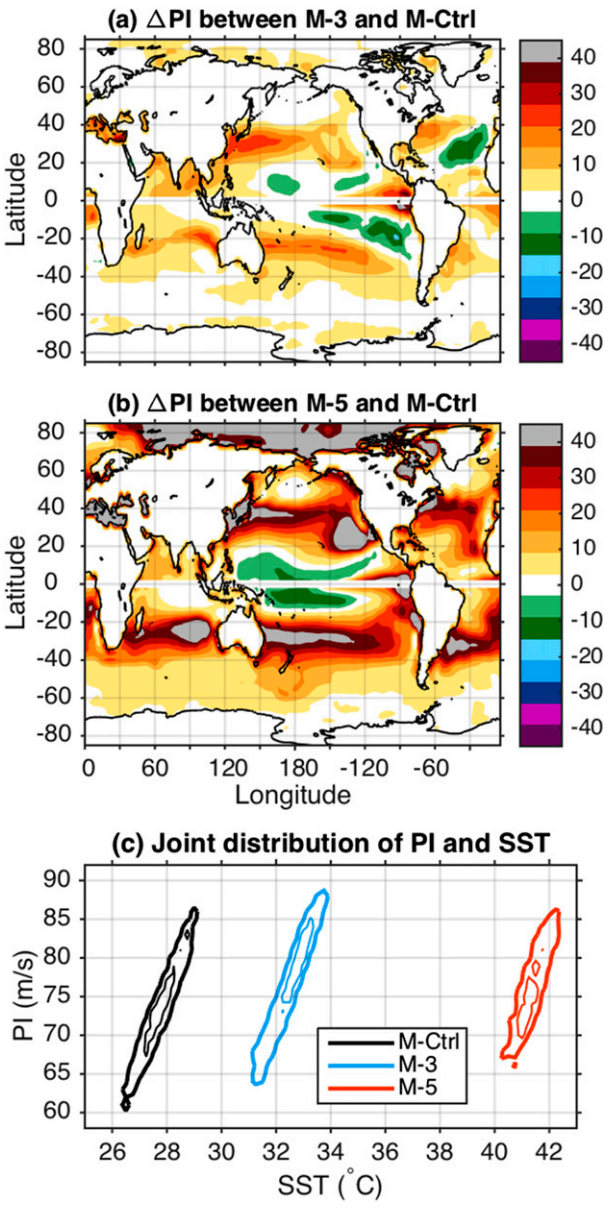

FIG. 7. Difference in storm-season mean (July–October for Northern Hemisphere; January–April for Southern Hemisphere) of PI ($\mathrm{m\,s^{-1}}$) (a) between M-3 and M-Ctrl and (b) between M-5 and M-Ctrl. (c) Joint distribution of potential intensity and SST for all points between 0° and 20°N from July to October for M-Ctrl (black), M-3 (blue), and M-5 (red); see text for further details.

$$V_{\mathrm{PI}}^2 = \frac{C_k}{C_D}\varepsilon(k_0^* - k_a), \tag{2}$$

where C_k and C_D are the exchange coefficients for enthalpy and momentum, ε is the thermodynamic efficiency (modified to account for dissipative heating; see Bister and Emanuel 2002), k_0^* is the saturation enthalpy of the sea surface, and k_a is the enthalpy of the ambient boundary

[4] Intense storms that travel into regions with low PI may persist for a short period of time, however, before the unfavorable environmental conditions into which the system moved have the ability to weaken or kill it.

[5] But our results are not sensitive to other sensible choices (e.g., June–November for the Northern Hemisphere or December–March for the Southern Hemisphere).

layer. If the upper ocean is in steady state and there is no convergence of heat flux within the upper ocean, then there is surface energy balance, which can be written

$$C_k \rho_a |V| (k_0^* - k_a) = F_{\text{solar}} + F_{\text{IR}}, \tag{3}$$

where ρ_a is the surface air density, $|V|$ is the average near-surface wind speed, F_{solar} is the net solar radiative flux into the sea, and F_{IR} is the net infrared flux into the sea. Combining (2) and (3) gives

$$V_{\text{PI}}^2 = \frac{\varepsilon (F_{\text{solar}} + F_{\text{IR}})}{C_D \rho_a |V|}. \tag{4}$$

As the net infrared opacity of the atmosphere becomes larger with increasing CO_2, the net infrared flux into the sea tends toward zero. (The effective downward emission altitude becomes small.) Thus, an upper bound on PI is achieved when F_{IR} vanishes in (4):

$$V_{\text{PI}}^2 = \frac{\varepsilon F_{\text{solar}}}{C_D \rho_a |V|}. \tag{5}$$

Emanuel and Sobel (2013) ran experiments with a single-column model (and slab ocean) to radiative–convective equilibrium and showed that PI asymptotes in response to increasing CO_2 beyond about 32°C. Figure 7c, which plots the joint distribution of SST and PI between the equator and 20°N for all points during July–October,[6] shows similar behavior: the distribution of tropical PI values rise from M-Ctrl to M-3 but then is no higher at M-5 despite the very hot surface conditions in that simulation.

b. *Thermodynamic resistance parameter*

Another thermodynamic property that aids TCs is high levels of midtropospheric humidity; high values reduce the moisture flux necessary to saturate the column and render mixing of environmental air to be less toxic to maintaining moist convection. (Entraining drier environmental air lowers the entropy in the column further below its value at saturation.) Relative humidity has been shown to be nearly invariant with climate change, which means that though specific humidity q increases with temperature, so too does the gap between it and its value at saturation. This introduces an important inhibition to TC formation with warming: the moisture fluxes required to saturate a column must fill a gap that grows exponentially with temperature, following the Clausius–Clapeyron relation. Indeed, simulations by Nolan and Rappin (2008) and Rappin et al. (2010) revealed that the time required to form a TC increased with surface temperature and that a developing storm was more susceptible to being overwhelmed by environmental air entrainment in the presence of wind shear in warmer environments.

Emanuel (1995) first identified a nondimensional parameter that has proven useful in measuring the thermodynamic resistance to TCs:

$$\chi = \frac{s^* - s}{s_0^* - s^*}, \tag{6}$$

where s is the pressure-weighted moist entropy of the free troposphere and s^* and s_0^* are the saturation entropies of the free troposphere (pressure-weighted average) and at the sea surface, respectively.[7] By computing the numerator over the full depth of the troposphere, it is related to the time scale for convection to saturate the troposphere. Thus χ is the ratio of this to the time scale for surface fluxes to bring the troposphere into thermodynamic equilibrium with the sea surface (Emanuel 2013); it is a measure of thermodynamic resistance in that the quantity increases when surface fluxes weaken and/or saturation deficits aloft rise.

This resistance parameter increases with warming: it is larger in simulations of the twenty-first century (Emanuel et al. 2008; Emanuel 2010) and lower in the colder ones of the Last Glacial Maximum (Korty et al. 2012a). Figure 8 shows the numerator and denominator of (2) averaged over the storm seasons for each hemisphere. Both the numerator and denominator of χ increase significantly in the two warmer climate simulations relative to their magnitudes in M-Ctrl, but the numerator increases with warming faster than the denominator. This behavior is consistent with that of climate projections in models of the next century (e.g., Emanuel et al. 2010): as relative humidity is relatively invariant across climates, the numerator increases exponentially with temperature, but surface disequilibrium increases more slowly. The fluxes that supply moisture via convection to the middle troposphere increase more slowly than does the demand placed by growing saturation deficits with temperature. This has consequences in the presence of vertical wind shears, which mix the drier environmental air into the saturated core of TCs (Tang and Emanuel 2012); we analyze these next.

[6] The joint distribution was calculated by binning all PI values from points between 0° and 20°N from the four long-term monthly means (July–October) into 1 m s^{-1} increments and all SSTs into 0.25°C increments. In Fig. 7c, thick lines encircle all regions of the joint distribution with at least 25 points, and thin lines encircle those with at least 75 points.

[7] Alternatively, the moist entropies can be replaced with moist static energies, which are generally easier to compute from data in height coordinates. We use the entropy form here and compute these following the same details outlined in Korty and Schneider (2007) and Zamora et al. (2016) for saturation equivalent potential temperatures.

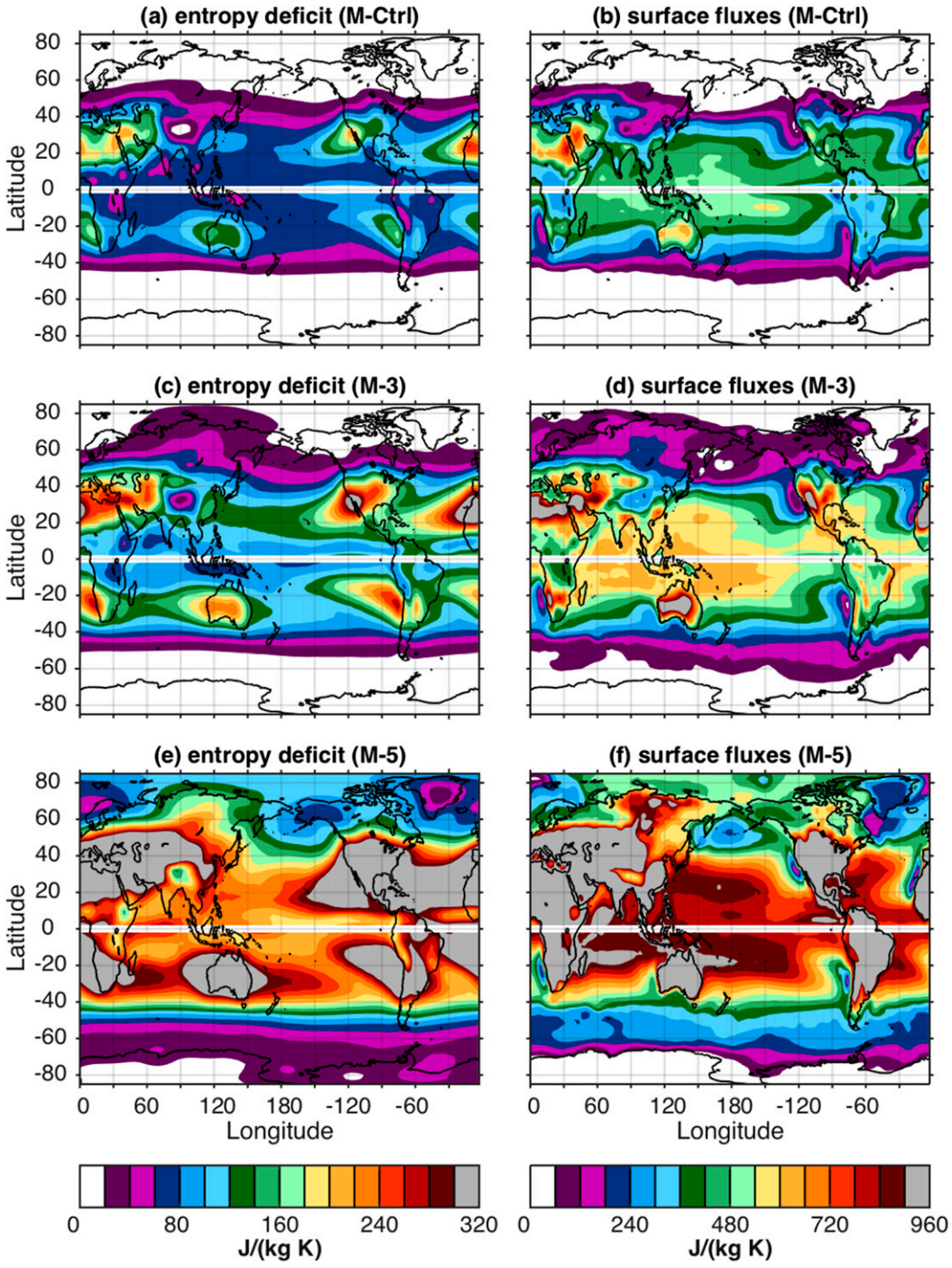

FIG. 8. Storm-season mean value of (left) numerator and (right) denominator of thermodynamic resistance parameter χ in (a),(b) M-Ctrl, (c),(d) M-3, and (e),(f) M-5.

c. Vertical wind shear and the ventilation parameter

Figures 9a,c,e show the magnitude of the 850–250-hPa vertical wind shear vector (hereafter, shear) averaged over peak months of each hemisphere's storm season. The mean values are generally low across a wide swath of the tropics but somewhat higher in the north Indian Ocean, where shears are larger during midsummer. The magnitude of the shear decreases in the warmer climate experiments through most of the tropics, particularly in

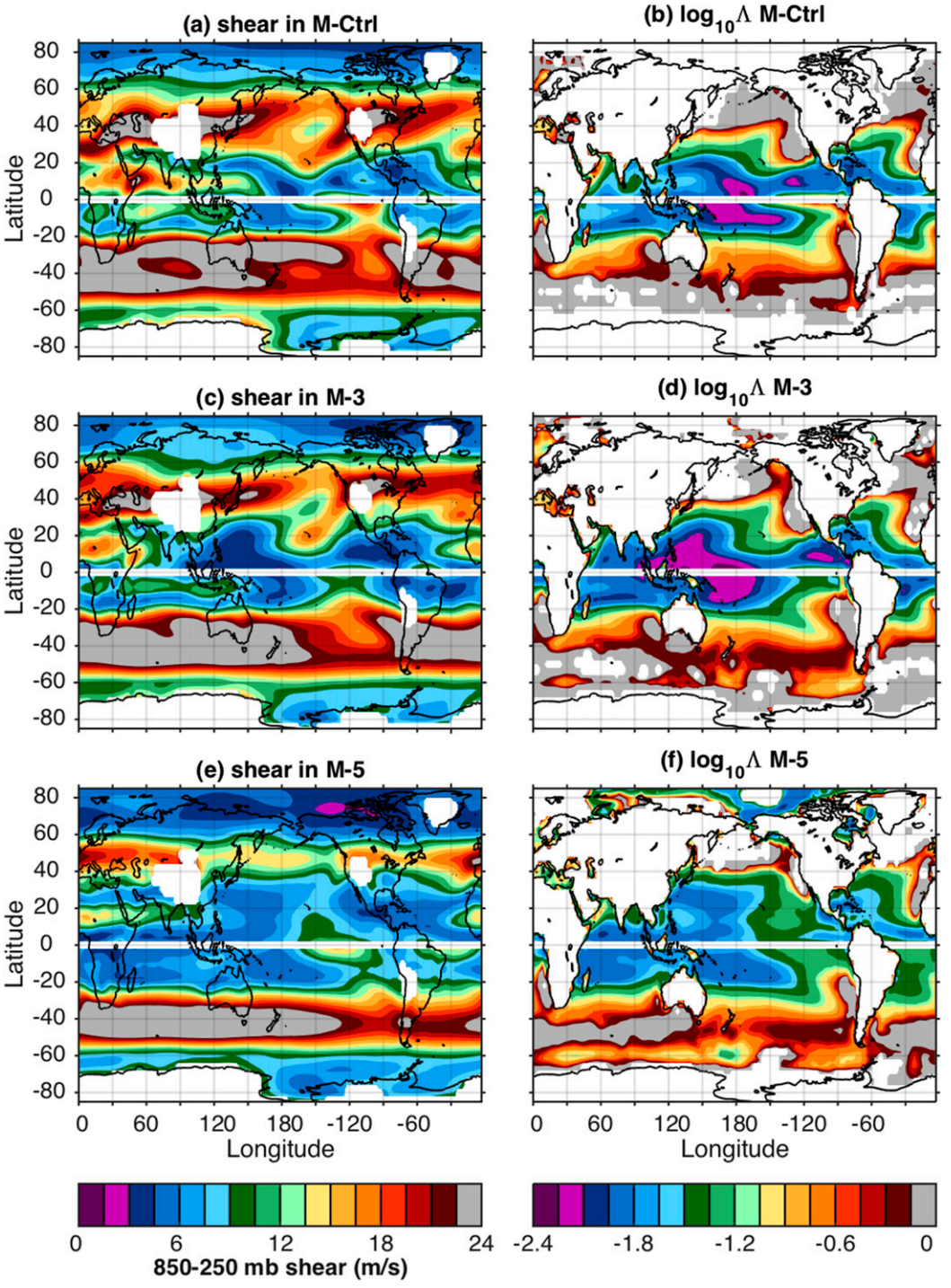

FIG. 9. Storm-season mean values of (left) magnitude of 850–250-hPa wind shear vector (1 mb = 1 hPa) and (right) the logarithm of nondimensional ventilation index in (a),(b) M-Ctrl, (c),(d) M-3, and (e),(f) M-5.

the Indian Ocean and western North Pacific, while it rises modestly in the central Pacific. The region of low tropical shears expands into the midlatitudes in the warmest case, with mean shears less than $10\,\mathrm{m\,s^{-1}}$ expanding poleward to 40°N in M-5.

The declines in mean tropical wind shear and expansion of low values to higher latitudes are important in their own right, but they are especially important through coupling with the thermodynamic variables examined in the previous section. Tang and

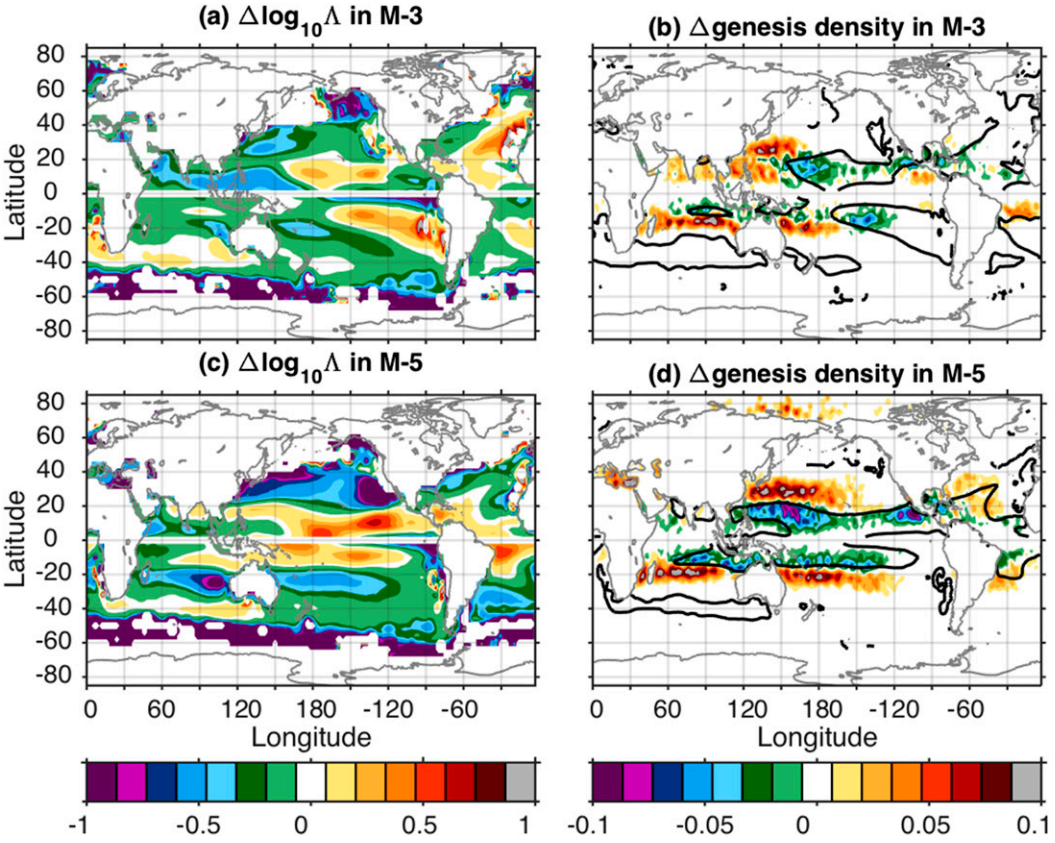

FIG. 10. (a) Difference in logarithm of normalized wind shear between M-3 and M-Ctrl during each hemisphere's storm season. (b) Difference in storm-season genesis density between M-3 and M-Ctrl (color) and contour line of zero change in logarithm of normalized wind shear (black) from (a). (c) As in (a), but for M-5. (d) As in (b), but for M-5 with the zero change in normalized wind shear from (c).

Emanuel (2010, 2012) showed that a normalized wind shear, called the ventilation parameter, reduces the intensity that a cyclone can achieve when subsaturated environmental air is entrained through deep-tropospheric shear. They defined a nondimensional ventilation index Λ:

$$\Lambda = \frac{V_{\rm sh}}{V_{\rm PI}}\chi, \tag{7}$$

where $V_{\rm sh}$ is the magnitude of the tropospheric wind shear vector (here computed using the 850–250-hPa levels), $V_{\rm PI}$ is the potential intensity calculated from (2), and χ is the thermodynamic resistance parameter given by (6). Like shear, regions with low values are preferential for TCs. Figures 9b,d,f show values from (7) averaged across each hemisphere's season of the three climates. [Because small values from (7) can be challenging to distinguish, we follow the practice of Tang and Emanuel (2012) and show the logarithm of Λ instead.] Two characteristics, both qualitatively consistent with the changes in TC climatology reported in the last section, are noteworthy in the warmer climates. First, the low values of Λ expand poleward with warming; second, low-latitude values are in many regions higher in the warmer climates than in M-Ctrl.

These changes are a bit easier to see in difference plots; Figs. 10a,c show the difference in $\log_{10}\Lambda$ in the two warmer climates. Figures 10b,d show the alignment of differences in genesis density[8] in the two warmer climates with changes in the storm-season mean Λ. Regions where conditions have combined to be less favorable ($\Delta\Lambda > 0$) are well aligned with the locations where the frequency of genesis has declined. The decrease in genesis density and increase in normalized shear at many of the lowest latitudes is consistent with the behavior reported by Rappin et al. (2010), who

[8] The changes in genesis density shown in Figs. 10b and 10d differ slightly from the changes shown in Figs. 3a and 3c because the data in Fig. 10 are restricted to the storm seasons only, while data in Fig. 3 are from the entire year.

showed that the time scale for TC formation in a radiative–convective equilibrium environment increased with surface temperature for fixed wind shear. (It scales with the same nondimensional number Λ, which they called an incubation parameter.) The reason is that a fixed magnitude of shear entrains air with a larger saturation deficit in warmer environments (if relative humidity is also constant), while the surface fluxes needed to moisten the column increase too slowly with temperature to close the growing gap between the actual specific humidity and its value at saturation. This means that weak, incipient storms have a larger hurdle to overcome, and several experiments with higher levels of shear failed to develop at all above higher surface temperatures (Rappin et al. 2010). The results shown in Fig. 10 suggest that conditions become more resistant to TCs in deep tropical latitudes with warming but that a poleward expansion of the generally favorable tropical environment opens previously hostile territory in subtropical and higher latitudes to TC formation in these experiments. This is consistent with the expansion of the tropics seen in some projections of the next century, albeit to a larger degree in the climates studied here.

5. Discussion

We found that the frequency, lifetime, and latitudes in which storms form and travel increase when global models with carbon dioxide levels higher than studied to date are downscaled using the method developed by Emanuel (2006). In an experiment with $8 \times CO_2$, the number of the most severe category 5 storms increases 52% and the amount of power dissipated rises 14%, but some regions of the deep tropics begin to experience reduced activity as conditions become more hostile with increasing ventilation. This trend becomes dominant in an experiment with $32 \times CO_2$: large areas equatorward of 20° latitude feature very large saturation deficits, which in the presence of robust wind shear and potential intensity values no larger than in today's climate, become more frequently lethal to incipient vortices. In both of the high-CO_2 experiments, TC activity spreads to new territory in the subtropics and midlatitudes as environmental conditions turn increasingly favorable there. Genesis, tracks, and the latitude at which storms reach their peak intensity and dissipate the most power all move poleward as warming increases further. The increase in storm genesis, tracks, and power dissipation in the subtropics and higher latitudes and the regional declines in the deep tropics are consistent with local changes in the ventilation index (Tang and Emanuel 2010, 2012).

The changes reported here are broadly in line with the results of this same method applied to the smaller warming in CMIP5 models (Emanuel 2013), and they are aligned with global and regional changes in environmental factors known to influence their climatology. The results of the $32 \times CO_2$ experiment show that if environmental conditions become harsh enough (e.g., large saturation deficits without compensating increases in PI or decreases in shear), TC activity can decline. Yet even as the number of all categories of hurricanes declined in the $32 \times CO_2$ experiment, the rare events that exceed 190 kt became more than twice as likely.

Our results show that the several aspects of the response of this method of downscaling TCs to a warming climate reported in Emanuel (2013) continue with larger departures from the modern climate. Emanuel (2013) reported that downscaling a later generation of the same model used here (CCSM4; we use CAM3.0) yielded an increase in storm frequency of 11%, and an increase in global power dissipation of 8% in the representative concentration pathway 8.5 (RCP8.5) scenario of CMIP5 compared to modern day. We find that the frequency continues to grow with higher levels of CO_2 by 16% in M-3 and by 20% in M-5, although this comes principally from an expansion to higher latitudes as conditions become too harsh in the deep tropics of the hottest case. We find that power dissipation increases by 14% in M-3 but declines 25% in M-5. Zonally integrated PDI becomes significant in the midlatitudes in M-5, while it declines in tropical latitudes.

The poleward shift in power dissipation raises interesting questions about possible feedbacks between TCs and climate through the ocean's thermal response to and recovery from a storm's passage (Sriver et al. 2008; Korty et al. 2008; Sriver and Huber 2007, 2010; Federov et al. 2010). Although the amount of ocean heat transported to distant locations may be constrained by a local recycling (Pasquero and Emanuel 2008; Jansen and Ferrari 2009; Mei and Pasquero 2012), other local feedbacks might augment aspects of the TC climatology further through warmer upper-ocean profiles or a permanent El Niño state (Sriver and Huber 2010; Federov et al. 2010; Sriver et al. 2013). These interactions, absent in the simulations examined here, have the potential to amplify some of the responses to warming that we found further still.

The response of this method may be contrasted with that of explicitly tracked systems in global models (cf. Camargo and Wing 2016; Walsh et al. 2016), which generally decline in frequency with twenty-first-century levels of warming, although there is considerable variability in their response from model to model (Camargo 2013) and, possibly, from different tracking algorithms

(Horn et al. 2014). Some of this difference may be related to the survival of weaker tropical storms: many tracking algorithms tend to identify fewer in warmer climates, while we find a robust increase here. On the other hand, some possible feedbacks between the TCs and climate that are not possible with the downscaling technique used here might constrain the number of events in interactive models. For example, there is evidence that the separation between storms in radiative–convective equilibrium models increases with warming (Khairoutdinov and Emanuel 2013), and changes in the climatology of precursor disturbances may be important as well. The poleward expansion of favorable environmental conditions also raises the question of whether genesis pathways may change. Here, storms can form from randomly supplied initial vortices, but how the climatology of precursor events may differ in an atmosphere with $32 \times CO_2$ remains an unexplored question. We feel that paleoclimate simulations are useful tools for studying how each of the techniques employed to study TCs and climate behave over the much larger climate changes they offer.

Our findings indicate that even if the climatology of TCs were to change little with climate in areas where they exist in modern times, potentially significant changes can come with an expansion of tropical air masses that may arise from changes to the general circulation. These results show that warm periods support stronger TCs over much larger areas, which could make important contributions to ocean mixing. A weakly stratified early Cenozoic ocean might have featured much stronger mixing rates than modern periods, as suggested by a comparison of numerical simulations and the water mass properties inferred from neodymium-derived proxies of the period (Thomas et al. 2014). These shifts also have potential relevance to future periods, and evidence that several characteristics of the TC climatology are shifting poleward (Kossin et al. 2014, 2016) may prove to be just as significant as any changes to the climatology within tropical latitudes.

Acknowledgments. We thank Timothy Merlis and an anonymous reviewer for thoughtful comments on an earlier draft of this manuscript. This work was supported by National Science Foundation Grants AGS-1064013, AGS-0902780, and OCE-0902882.

REFERENCES

Adam, O., T. Schneider, and N. Harnik, 2014: Role of changes in mean temperatures versus temperature gradients in the recent widening of the Hadley circulation. *J. Climate*, **27**, 7450–7461, doi:10.1175/JCLI-D-14-00140.1.

Barnes, E. A., and L. Polvani, 2013: Response of the midlatitude jets, and of their variability, to increased greenhouse gases in the CMIP5 models. *J. Climate*, **26**, 7117–7135, doi:10.1175/JCLI-D-12-00536.1.

Bister, M., and K. A. Emanuel, 1998: Dissipative heating and hurricane intensity. *Meteor. Atmos. Phys.*, **65**, 233–240, doi:10.1007/BF01030791.

——, and ——, 2002: Low frequency variability of tropical cyclone potential intensity: 1. Interannual to interdecadal variability. *J. Geophys. Res.*, **107**, 4801, doi:10.1029/2001JD000776.

Caballero, R., and M. Huber, 2010: Spontaneous transition to superrotation in warm climates simulated by CAM3. *Geophys. Res. Lett.*, **37**, L11701, doi:10.1029/2010GL043468.

——, and ——, 2013: State-dependent climate sensitivity in past warm climates and its implications for future climate projections. *Proc. Natl. Acad. Sci. USA*, **110**, 14 162–14 167, doi:10.1073/pnas.1303365110.

Camargo, S. J., 2013: Global and regional aspects of tropical cyclone activity in the CMIP5 models. *J. Climate*, **26**, 9880–9902, doi:10.1175/JCLI-D-12-00549.1.

——, and A. A. Wing, 2016: Tropical cyclones in climate models. *Wiley Interdiscip. Rev.: Climate Change*, **7**, 211–237, doi:10.1002/wcc.373.

——, A. H. Sobel, A. G. Barnston, and K. A. Emanuel, 2007: Tropical cyclone genesis potential index in climate models. *Tellus*, **59A**, 428–443, doi:10.1111/j.1600-0870.2007.00238.x.

Cheng, L., F. Zheng, and J. Zhu, 2015: Distinctive ocean interior changes during the recent warming slowdown. *Sci. Rep.*, **5**, 14346, doi:10.1038/srep14346.

Emanuel, K. A., 1986: An air–sea interaction theory for tropical cyclones. Part I: Steady-state maintenance. *J. Atmos. Sci.*, **43**, 585–605, doi:10.1175/1520-0469(1986)043<0585:AASITF>2.0.CO;2.

——, 1987: The dependence of hurricane intensity on climate. *Nature*, **326**, 483–485, doi:10.1038/326483a0.

——, 1995: The behavior of a simple hurricane model using a convective scheme based on subcloud-layer entropy equilibrium. *J. Atmos. Sci.*, **52**, 3960–3968, doi:10.1175/1520-0469(1995)052<3960:TBOASH>2.0.CO;2.

——, 2006: Climate and tropical cyclone activity: A new model downscaling approach. *J. Climate*, **19**, 4797–4802, doi:10.1175/JCLI3908.1.

——, 2010: Tropical cyclone activity downscaled from NOAA-CIRES reanalysis, 1908–1958. *J. Adv. Model. Earth Syst.*, **2**, 1, doi:10.3894/JAMES.2010.2.1.

——, 2013: Downscaling CMIP5 climate models shows increased tropical cyclone activity over the 21st century. *Proc. Natl. Acad. Sci. USA*, **110**, 12 219–12 224, doi:10.1073/pnas.1301293110.

——, and A. Sobel, 2013: Response of tropical sea surface temperature, precipitation, and tropical cyclone–related variables to changes in global and local forcing. *J. Adv. Model. Earth Syst.*, **5**, 447–458, doi:10.1002/jame.20032.

——, C. DesAutels, C. Holloway, and R. Korty, 2004: Environmental control of tropical cyclone intensity. *J. Atmos. Sci.*, **61**, 843–858, doi:10.1175/1520-0469(2004)061<0843:ECOTCI>2.0.CO;2.

——, R. Sundararajan, and J. Williams, 2008: Hurricanes and global warming: Results from downscaling IPCC AR4 simulations. *Bull. Amer. Meteor. Soc.*, **89**, 347–367, doi:10.1175/BAMS-89-3-347.

——, K. Oouchi, M. Satoh, H. Tomita, and Y. Yamada, 2010: Comparison of explicitly simulated and downscaled tropical cyclone activity in a high-resolution global climate model. *J. Adv. Model. Earth Syst.*, **2**, 9, doi:10.3894/JAMES.2010.2.9.

Fedorov, A. V., C. M. Brierley, and K. Emanuel, 2010: Tropical cyclones and permanent El Niño in the early Pliocene epoch. *Nature*, **463**, 1066–1070, doi:10.1038/nature08831.

Gray, W. M., 1968: Global view of the origin of tropical disturbances and storms. *Mon. Wea. Rev.*, **96**, 669–700, doi:10.1175/1520-0493(1968)096<0669:GVOTOO>2.0.CO;2.

——, 1979: Hurricanes: Their formation, structure and likely role in the tropical circulation. *Meteorology over Tropical Oceans*, D. B. Shaw, Ed., Royal Meteorological Society, 155–218.

Holland, G., and C. L. Bruyère, 2014: Recent intense hurricane response to global climate change. *Climate Dyn.*, **42**, 617–627, doi:10.1007/s00382-013-1713-0.

Horn, M., and Coauthors, 2014: Tracking scheme dependence of simulated tropical cyclone response to idealized climate simulations. *J. Climate*, **27**, 9197–9213, doi:10.1175/JCLI-D-14-00200.1.

Hoyos, C. D., and P. J. Webster, 2012: Evolution and modulation of tropical heating from the last glacial maximum through the twenty-first century. *Climate Dyn.*, **38**, 1501–1519, doi:10.1007/s00382-011-1181-3.

Hu, Y., and Q. Fu, 2007: Observed poleward expansion of the Hadley circulation since 1979. *Atmos. Chem. Phys.*, **7**, 5229–5236, doi:10.5194/acp-7-5229-2007.

Hudson, R. D., M. F. Andrade, M. B. Follette, and A. D. Frolov, 2006: The total ozone field separated into meteorological regimes—Part II: Northern Hemisphere mid-latitude total ozone trends. *Atmos. Chem. Phys.*, **6**, 5183–5191, doi:10.5194/acp-6-5183-2006.

Jansen, M., and R. Ferrari, 2009: Impact of the latitudinal distribution of tropical cyclones on ocean heat transport. *Geophys. Res. Lett.*, **36**, L06604, doi:10.1029/2008GL036796.

Johnson, N. C., and S.-P. Xie, 2010: Changes in the sea surface temperature threshold for tropical convection. *Nat. Geosci.*, **3**, 842–845, doi:10.1038/ngeo1008.

Khairoutdinov, M., and K. Emanuel, 2013: Rotating radiative–convective equilibrium simulated by a cloud-resolving model. *J. Adv. Model. Earth Syst.*, **5**, 816–825, doi:10.1002/2013MS000253.

Knutson, T. R., J. J. Sirutis, M. Zhao, R. E. Tuleya, M. Bender, G. A. Vecchi, G. Villarini, and D. Chavas, 2015: Global projections of intense tropical cyclone activity for the late twenty-first century from dynamical downscaling of CMIP5/RCP4.5 scenarios. *J. Climate*, **28**, 7203–7224, doi:10.1175/JCLI-D-15-0129.1.

Koh, J. H., and C. M. Brierley, 2015: Tropical cyclone genesis potential across palaeoclimates. *Climate Past*, **11**, 1433–1451, doi:10.5194/cp-11-1433-2015.

Korty, R. L., and K. A. Emanuel, 2007: The dynamic response of the winter stratosphere to an equable climate surface temperature gradient. *J. Climate*, **20**, 5213–5228, doi:10.1175/2007JCLI1556.1.

——, and T. Schneider, 2007: A climatology of the tropospheric thermal stratification using saturation potential vorticity. *J. Climate*, **20**, 5977–5991, doi:10.1175/2007JCLI1788.1.

——, K. A. Emanuel, and J. R. Scott, 2008: Tropical cyclone–induced upper-ocean mixing and climate: Application to equable climates. *J. Climate*, **21**, 638–654, doi:10.1175/2007JCLI1659.1.

——, S. J. Camargo, and J. Galewsky, 2012a: Tropical cyclone genesis factors in simulations of the Last Glacial Maximum. *J. Climate*, **25**, 4348–4365, doi:10.1175/JCLI-D-11-00517.1.

——, ——, and ——, 2012b: Variations in tropical cyclone genesis factors in simulations of the Holocene epoch. *J. Climate*, **25**, 8196–8211, doi:10.1175/JCLI-D-12-00033.1.

Kossin, J. P., K. A. Emanuel, and G. A. Vecchi, 2014: The poleward migration of the location of tropical cyclone maximum intensity. *Nature*, **509**, 349–352, doi:10.1038/nature13278.

——, ——, and S. J. Camargo, 2016: Past and projected changes in western North Pacific tropical cyclone exposure. *J. Climate*, **29**, 5725–5739, doi:10.1175/JCLI-D-16-0076.1.

Lucas, C., B. Timbal, and H. Nguyen, 2014: The expanding tropics: A critical assessment of the observational and modeling studies. *Wiley Interdiscip. Rev.: Climate Change*, **5**, 89–112, doi:10.1002/wcc.251.

Mbengue, C., and T. Schneider, 2013: Storm track shifts under climate change: What can be learned from large-scale dry dynamics. *J. Climate*, **26**, 9923–9930, doi:10.1175/JCLI-D-13-00404.1.

Mei, W., and C. Pasquero, 2012: Restratification of the upper ocean after the passage of a tropical cyclone: A numerical study. *J. Phys. Oceanogr.*, **42**, 1377–1401, doi:10.1175/JPO-D-11-0209.1.

——, F. Primeau, J. C. McWilliams, and C. Pasquero, 2013: Sea surface height evidence for long-term warming effects of tropical cyclones on the ocean. *Proc. Natl. Acad. Sci. USA*, **110**, 15 207–15 210, doi:10.1073/pnas.1306753110.

Murakami, H., and Coauthors, 2015: Simulation and prediction of category 4 and 5 hurricanes in the high-resolution GFDL HiFLOR coupled climate model. *J. Climate*, **28**, 9058–9079, doi:10.1175/JCLI-D-15-0216.1.

Nolan, D. S., and E. D. Rappin, 2008: Increased sensitivity of tropical cyclogenesis to wind shear in higher SST environments. *Geophys. Res. Lett.*, **35**, L14805, doi:10.1029/2008GL034147.

O'Gorman, P. A., and T. Schneider, 2008: The hydrological cycle over a wide range of climates simulated with an idealized GCM. *J. Climate*, **21**, 3815–3832, doi:10.1175/2007JCLI2065.1.

Pasquero, C., and K. Emanuel, 2008: Tropical cyclones and transient upper-ocean warming. *J. Climate*, **21**, 149–162, doi:10.1175/2007JCLI1550.1.

Price, J. F., 1981: Upper ocean response to a hurricane. *J. Phys. Oceanogr.*, **11**, 153–175, doi:10.1175/1520-0485(1981)011<0153:UORTAH>2.0.CO;2.

Rappin, E. D., D. S. Nolan, and K. A. Emanuel, 2010: Thermodynamic control of tropical cyclogenesis in environments of radiative–convective equilibrium with shear. *Quart. J. Roy. Meteor. Soc.*, **136**, 1954–1971, doi:10.1002/qj.706.

Seidel, D. J., and W. J. Randel, 2007: Recent widening of the tropical belt: Evidence from tropopause observations. *J. Geophys. Res.*, **112**, D20113, doi:10.1029/2007JD008861.

——, Q. Fu, W. J. Randel, and T. J. Reichler, 2008: Widening of the tropical belt in a changing climate. *Nat. Geosci.*, **1**, 21–24, doi:10.1038/ngeo.2007.38.

Sherwood, S. C., and M. Huber, 2010: An adaptability limit to climate change due to heat stress. *Proc. Natl. Acad. Sci. USA*, **107**, 9552–9555, doi:10.1073/pnas.0913352107.

Simpson, I. R., T. A. Shaw, and R. Seager, 2014: A diagnosis of the seasonally and longitudinally varying midlatitude circulation response to global warming. *J. Atmos. Sci.*, **71**, 2489–2515, doi:10.1175/JAS-D-13-0325.1.

Sobel, A. H., S. J. Camargo, T. M. Hall, C.-Y. Lee, M. K. Tippett, and A. A. Wing, 2016: Human influence on tropical cyclone intensity. *Science*, **353**, 242–246, doi:10.1126/science.aaf6574.

Sriver, R. L., and M. Huber, 2007: Observational evidence for an ocean heat pump induced by tropical cyclones. *Nature*, **447**, 577–580, doi:10.1038/nature05785.

——, and ——, 2010: Modeled sensitivity of upper thermocline properties to tropical cyclone winds and possible feedbacks on the Hadley circulation. *Geophys. Res. Lett.*, **37**, L08704, doi:10.1029/2010GL042836.

——, ——, and J. Nusbaumer, 2008: Investigating tropical cyclone-climate feedbacks using the TRMM Microwave Imager and the Quick Scatterometer. *Geochem. Geophys. Geosyst.*, **9**, Q09V11, doi:10.1029/2007GC001842.

——, ——, and L. Chafik, 2013: Excitation of equatorial Kelvin and Yanai waves by tropical cyclones in an ocean general circulation model. *Earth Syst. Dyn.*, **4**, 1–10, doi:10.5194/esd-4-1-2013.

Tang, B., and K. Emanuel, 2010: Midlevel ventilation's constraint on tropical cyclone intensity. *J. Atmos. Sci.*, **67**, 1817–1830, doi:10.1175/2010JAS3318.1.

——, and ——, 2012: A ventilation index for tropical cyclones. *Bull. Amer. Meteor. Soc.*, **93**, 1901–1912, doi:10.1175/BAMS-D-11-00165.1.

Thomas, D. J., R. Korty, M. Huber, J. A. Schubert, and B. Haines, 2014: Nd isotopic structure of the Pacific Ocean 70–30 Ma and numerical evidence for vigorous ocean circulation and ocean heat transport in a greenhouse world. *Paleoceanography*, **29**, 454–469, doi:10.1002/2013PA002535.

Vecchi, G. A., and B. J. Soden, 2007: Effect of remote sea surface temperature change on tropical cyclone potential intensity. *Nature*, **450**, 1066–1070, doi:10.1038/nature06423.

Walsh, K. J. E., and Coauthors, 2016: Tropical cyclones and climate change. *Wiley Interdiscip. Rev.: Climate Change*, **7**, 65–89, doi:10.1002/wcc.371.

Williams, I. N., R. T. Pierrehumbert, and M. Huber, 2009: Global warming, convective threshold and false thermostats. *Geophys. Res. Lett.*, **36**, L21805, doi:10.1029/2009GL039849.

Yan, Q., R. Korty, and Z. Zhang, 2015: Tropical cyclone genesis factors in a simulation of the last two millennia: Results from the Community Earth System Model. *J. Climate*, **28**, 7182–7202, doi:10.1175/JCLI-D-15-0054.1.

Zamora, R. A., R. L. Korty, and M. Huber, 2016: Thermal stratification in simulations of warm climates: A climatology using saturation potential vorticity. *J. Climate*, **29**, 5083–5102, doi:10.1175/JCLI-D-15-0785.1.